Potential Controlled Electrochemical Conversion of AgCN and $Cu(OH)_2$ Nanofibers into Metal Nanoparticles, Nanoprisms, Nanofibers, and Porous Networks

Gilles R. Bourret and R. Bruce Lennox*

Department of Chemistry and Center for Self-Assembled Chemical Structures (CSACS), McGill University, 801 Sherbrooke Street W, Montreal, Quebec H3A 2K6, Canada

ABSTRACT Nanowires are expected to provide considerable advances in the use of smaller and more efficient sensing, electronic, and photovoltaic devices. Good electrical connections of the nanowires within devices can, however, be problematic. We present here a new method that takes advantage of the available large-scale and reproducible wet-chemical syntheses of non-zero-valent anisotropic nanomaterials. The electrochemical reduction of preformed solid AgCN and $Cu(OH)_2$ nanofibers (NFs) on surfaces allows one to form metallic nanostructures that are integrated in electrical junctions with excellent electrical contacts. Some fundamental aspects of the electrochemical reduction of AgCN NF are presented, including their redox potential and propagation of the metal boundary formed during the electrochemical reduction process. The clear connection between native (unreduced) AgCN NF and reduced Ag^0 nanostructures is shown. The reduction potential, the nature of the supporting substrate (conductive vs insulating), and the size of the original fibers strongly influence the morphology and dimensions of the Ag^0 nanostructures thus produced. A number of different Ag^0 nanostructures are electrosynthesized, including nanoprisms, nanoparticles (NPs), and NFs, made from the aggregation of nanoprisms and NPs, and continuous fibers, whose width is tunable between 90 and 500 nm. We report the formation of excellent electrical contact via the electrochemical reduction of metal/M^{z+} NF/metal junctions. This technique is simple, fast, and applicable to other materials such as $Cu(OH)_2$ NF. It allows for the formation of electrically connected metallic networks with new interesting geometries, which could be applied to a form of electrochemical welding.

KEYWORDS: silver • cyanide • copper • electrochemistry • nanowire • nanoprism

1. INTRODUCTION

Metal and semiconductor nanomaterials are of considerable interest because of their size-dependent properties (luminescence, absorption and scattering of light, conductivity, and catalytic activity) as well as their large surface-to-volume ratio (1). Sensors in particular benefit from nanoscale dimensions. The resulting drastic increase in the surface area is often linked to a strong enhancement of the sensing/physical output (conductivity, luminescence, light scattering, etc.) with decreasing material dimensions (2−5). A nanowire geometry is often envisioned to be an optimal geometry given that it can exhibit excellent electrical performance while being amenable to integration into electrical circuits (6). Good electrical connections of the nanowires within devices can, however, be problematic. For example, contacts between ZnO nanowires and the electrode terminals play a major role in the performance of ZnO nanowire devices (7). Simple and reliable methods to improve the electrical connections of nanowires and the circuit in which they are integrated are thus much sought-after.

The numerous methods to produce metallic nanowires include the use of hard templates (8), soft templates (9−13), or direct template-free synthesis (14−18). In all cases, zero-valent metallic nanostructure fabrication involves the reduction of a metal precursor M^{z+}. This electron transfer can be achieved via electrochemistry (19−21), thermal decomposition (11, 22−24), chemical reduction (25, 26), photogeneration of radicals (27), or nonconventional external high-energy electron sources (28−30). Electrochemistry is particularly attractive because it is inexpensive, reliable, and amenable to large-scale processing. Precise control of electron transfer through changes in the Fermi level of the working electrode (WE) offers considerable tunability in reduction conditions in both thermodynamic and kinetic terms.

The electrochemical reduction of soluble species to yield metallic, metal oxide, and metal complex nanostructures has been extensively studied in the past 15 years. For example, Pd and Ni nanoparticles (NPs) were synthesized via the electroreduction of Pd and Ni ions generated by the sacrificial oxidation of a Pd (Ni) anode in the presence of ammonium salts (19). The size of these clusters was tuned from 1.4 to 4.8 nm by changing the current density. The electrochemical deposition of Ag NP onto the basal plane of highly oriented pyrolytic graphite (HOPG) can be achieved using a potentiostatic pulse method (20). Highly monodisperse nanorods were synthesized via the electrochemical reduc-

* To whom correspondence should be addressed. E-mail: bruce.lennox@mcgill.ca.

Received for review September 26, 2010 and accepted November 8, 2010

DOI: 10.1021/am100924c

tion of Au ions generated by the oxidation of a Au anode using hexadecyltrimethylammonium bromide (HDMB) and tetraoctylammonium bromide (TOAB) as the electrolytes (21). The addition of acetone, expected to induce cylindrical aggregation of the HDMB−TOAB system, leads to rod formation. Micron-sized Ag_2O structures with unconventional shapes (such as flower and hopper morphologies) were synthesized in solution via the oxidation of a Ag wire in an aqueous basic solution (31), while electrodeposition was successfully used to form a wide variety of hierarchical ZnO nanostructures on surfaces (nanosheets, nanorods, 6-fold symmetry columns, hexagonal pillars, etc.) (32−34). Electrocrystallization of $M^{z+}(TCNQ^-)_z$ (M^{z+} = metal ion; TNCQ = tetracyanoquinodimethane) was recently demonstrated via the reduction of TCNQ in the presence of a metal salt. In these experiments, TCNQ was solubilized in acetonitrile or in an ionic liquid to form structures with controllable geometries (35, 36).

The electrochemical fabrication of two-dimensional (2D)-ordered metallic nanostructures on surfaces was pioneered by Penner and colleagues, involving the "HOPG step edge decoration" method. This method takes advantage of the atomic step edges of HOPG to template the reduction of metal ions into well-defined nanowires (37). Practical challenges include accessing the HOPG substrate required for the nanowire formation and developing a process to transfer the nanowires onto insulating surfaces to eventually make sensing devices. Recently, microfabrication processes coupled to electrodeposition allow for the patterning of metallic nanowires on dielectrics. These are multistep processes that require tools that are not widely available (38). Moreover, this technique produces nanowires composed of small metallic nanocrystals that can have undesirable conduction properties.

Instead of electrodepositing metals from soluble inorganic salts onto templating structures, we present here a new method that takes advantage of the available large-scale and reproducible wet-chemical syntheses of non-zero-valent anisotropic nanomaterials (9−13, 39−42). The electrochemical reduction of these preformed nanofibers (NFs) on surfaces allows us to form metallic nanostructures that are integrated in electrical junctions with excellent electrical contacts. To our knowledge, the electrochemical study of insoluble metal complexes was initiated by Bond and Scholz in the early 1990s (43). Their work established the electrochemical solid−solid transformation of insoluble TCNQ microcrystals into $M^{z+}(TCNQ^-)_z$ nanostructures (44, 45), as well as the electrochemical reduction of AgCl (43, 46) and Ag_2S (47) ionic microcrystals into metallic Ag^0 microstructures. As expected, the reduction of solid species occurs at the electrode/crystal/solvent interface (48). It proceeds via a nucleation-and-growth process, which significantly differs from diffusion-controlled reactions of soluble species. The boundary of this solid/solid/liquid interface moves as the crystal is progressively reduced. The decrease in the size of an Ag_2S microcrystal during its electroreduction into Ag^0 was studied by atomic force microscopy and was shown to be in excellent agreement with the theoretical value (47). Two main conclusions can be drawn from this work. First, the redox potentials of the solid species are usually very similar to that of the corresponding dissolved species, although an overpotential can be required to initiate the electroreduction. Second, the complete electrochemical transformation of ionic microcrystals (i.e., Ag_2S to Ag^0) into metallic microstructures can be achieved.

We present in this paper the electrochemical reduction of two materials that we have recently shown to be readily accessible using new template methods: AgCN[13] and $Cu(OH)_2$ (41). NFs of these materials lead to the formation of conductive metallic nanostructures on surfaces. Our extensive electrochemical understanding of the AgCN NF (13) allows us to establish the influence of the reduction potential (V_r), the nature of the supporting substrate (conductive vs insulating), and the size of the original fibers on the resulting Ag^0 nanostructures. By changing these parameters, we are able to control both the morphology and dimensions of the Ag^0 nanostructures produced, leading to nanoprisms, NPs, and NFs. Generalization of this technique is demonstrated by the electrochemical reduction of $Cu(OH)_2$ NF into a porous conductive network of Cu NF. Finally, we report the formation of excellent electrical contact by the reduction of metal/M^{z+} NF/metal junctions.

2. EXPERIMENTAL SECTION

2.1. Materials. Poly(styrene-*alt*-maleic anhydride) 50 kDa (SMA) was purchased from SP[2] Scientific Polymer Products. $AgNO_3$ (>99%), AgCN (>99%), $KAg(CN)_2$, NaCN (>99.98%), $KClO_4$ (>99.99%), $CuCl_2 \cdot 2H_2O$ (>99%), *n*-butylamine (>99.5%), and sodium cyanoborohydride were purchased from Sigma. All were used as-received. Pt-coated glass slides were purchased from Emtron Hybrids Inc. (Alberta Microelec). Graphite electrodes were made by de-laminating graphite rods (SPI Supplies, spectroscopic grade) with a razor blade. HOPG was purchased from SPI Supplies. Glass slides were obtained from Fisher.

2.2. Instruments. Scanning electron microscopy (SEM) images were obtained using a Hitachi S-4700 field-emission-gun scanning electron microscope operated at 5 kV. No visible deterioration of AgCN and $Cu(OH)_2$ NF under these conditions was observed. Energy-dispersive spectroscopy (EDS) measurements were performed on the same field-emission-gun scanning electron microscope using Oxford INCA EDS hardware. Typical conditions during the spectral acquisitions were as follows: size of the area analyzed, 5 μm; electron beam energy, between 6 and 10 kV; acquisition time, 90 s. Transmission electron microscopy (TEM) images were obtained using a Philips CM200 operated at 200 kV. Samples were drop-cast on Au TEM grids and C-coated Cu TEM grids (SPI Supplies).

2.3. AgCN−SMA NF Synthesis. SMA (50 kDa) nanotubes were synthesized as described previously (13). AgCN−SMA_{NaCN} NFs were synthesized via a modified version of our previously reported synthesis (13): 0.11 mmol of $AgNO_3$ dissolved in 7.5 mL of Milli-Q water was added to 7.5 mL of an aqueous SMA nanotube solution ($c = 2$ mg $\cdot$ mL^{-1}). Under slow stirring, 0.11 mmol of NaCN dissolved in 7.5 mL of Milli-Q water was added in one quick addition. The solution was slowly stirred for 40 h, before being centrifuged three times in 50 mL of ethanol. The resulting white fibers were kept in ethanol and stored, protected from the light, at room temperature. AgCN−SMA_{NaBH_3CN} NFs were synthesized as described previously from SMA nanotubes (50 kDa, $c = 2$ mg $\cdot$ mL^{-1}), $AgNO_3$, and $NaBH_3CN$ in the

presence of ambient oxygen and stored in Milli-Q water, protected from the light (13).

2.4. $Cu(OH)_2$ NF Synthesis. $Cu(OH)_2$ NFs were synthesized according to a two-phase synthesis that we recently published (41). Reactions were conducted in 30 mL vials (Fisherbrand) using a 1 cm stirring bar (Fisherbrand) under vigorous stirring (900 rpm). $CuCl_2 \cdot 2H_2O$ (0.4 mM) was dissolved in 5 mL of CH_2Cl_2 with 5 equiv of *n*-butylamine. A total of 5 mL of H_2O was added in one quick addition to the vial under stirring. After 5 min, the CH_2Cl_2 phase was immediately isolated with a separatory funnel and centrifuged three times in 50 mL of CH_2Cl_2. A blue product resulted. The fibers were kept in ca. 2 mL of CH_2Cl_2 before being drop-cast on the Au/glass/Au junctions.

2.5. Electrochemical Experiments. The electrochemical experiments were performed in a classic two-compartment electrochemical cell separated by a glass frit, using a 0.1 M $KClO_4$ aqueous electrolyte solution. A three-electrode setup was used, with a Pt counter electrode and an Ag/AgCl reference electrode, connected to a chi760c electrochemical workstation. We used $KClO_4$ as the conducting electrolyte because ClO_4^- weakly interacts with Ag (49), avoiding thus any parasitic anionic exchange within AgCN. All potentials are reported versus Ag/AgCl. Argon was bubbled for 30 min prior to any electrochemical experiment and was blown into the cell during the experiments. Before use, the electrochemical cell was thoroughly washed with H_2O and cleaned 30 min with a fresh piranha solution [3:1 mixture of concentrated hydrogen sulfuric acid (H_2SO_4) and hydrogen peroxide (H_2O_2)]. **Caution!** *A piranha solution is very reactive and can be explosive when combined with oxidizable material! Handle with care. It should never be in direct contact with significant amounts of organics.* The cell was then thoroughly rinsed with Milli-Q water and soaked in Milli-Q water for at least 30 min. Glassy carbon (GC) electrodes were carefully polished by using successively 1, 0.3, and 0.05 μm colloidal aluminum oxide, sonicated in Milli-Q water, and gently dried under dinitrogen. Although Bond and Scholz developed a protocol using a paraffin-coated graphite electrode to study the electrochemistry of insoluble compounds, we found that physical adsorption onto a GC electrode gives satisfactory results (43). The cleanliness of the GC electrodes was verified with cyclic voltammetry (CV) before use. AgCN−SMA and $Cu(OH)_2$ fibers were simply drop-cast onto the extremity of a clean GC electrode and left to dry at room temperature. The electrodes were quickly immersed (5−10 s) twice in 10 mL of Milli-Q water to remove any residual SMA, Na^+, CN^-, or $Ag(CN)_2^-$ prior to introduction into the electrochemical cell. In the case of pure AgCN, the GC electrode was rubbed onto a few mg of AgCN crystals, removing the excess AgCN with a Kimwipe and a gentle nitrogen flow. The potential window studied (−0.9 to +0.8 V vs Ag/AgCl) avoids cyanide polymerization into polycyanogens, which occurs below −1.1 V vs Ag/AgCl in 0.1 M $NaClO_4$ (50). Aqueous cyanide wastes were disposed of and stored in a basic KOH aqueous solution.

2.6. Au/M^0 Fibers/Au Junction Fabrication. Preliminary electrochemical reduction studies of NF networks were performed on glass slides (Fisher), which were half-coated with 5 nm Ti and then with 100 nm of Au using a metal evaporator. These Au films served as the WE. The AgCN−SMA fibers were drop-cast onto the glass/Au interface and electrolyzed at a constant potential (ranging from −0.3 to −0.9 V) for 20 min. Similar experiments were performed using Au/glass/Au junctions (cf. Scheme 1), with a glass domain width varying between 150 and 300 μm depending on the sample. Au/glass/Au junctions were similarly made using a thin Cu wire as a mask. The fibers were drop-cast onto the junctions, which were subsequently immersed twice in 10 mL of Milli-Q water to wash away any residual SMA, Na^+, CN^-, or $Ag(CN)_2^-$ prior to the electrolysis step at a constant potential. AgCN−SMA_{NaCN} NFs were drop-cast from an ethanol solution and AgCN−SMA_{NaBH_3CN} NFs from an aqueous solution. The junction was completely immersed in the electrolyte ($KClO_4$), while one Au electrode was electrically connected to the potentiostat. No significant dependence of the nanostructures produced on the size of the insulating glass gap was observed. To avoid electrochemical Ostwald ripening (51), the substrates were immediately removed from the solution at the end of the electrolysis step. After the electrolysis step, the substrates were quickly immersed (5−10 s) twice in 10 mL of Milli-Q water to remove any residual electrolyte and then dried under a nitrogen flow. No unreacted NFs were observed after potentiostatic electrolysis at $V_r \leq 0.55$ V and only occasionally after potentiostatic electrolysis at $V_r \geq -0.50$ V.

Scheme 1. Electrochemical Cell (Left)[a] and Schematic of the Au/AgCN−SMA NF/Au Junction (Right) before and after the Electrochemical Reduction (Not to Scale)

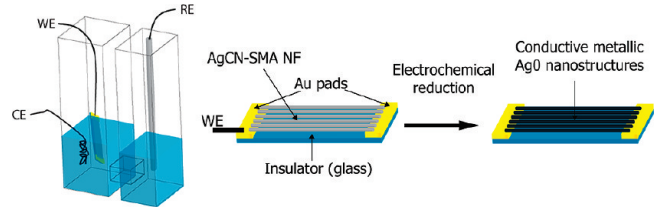

[a] WE: Au working electrode. RE: Ag/AgCl reference electrode. CE: Pt counter electrode.

Scheme 2. Schematic of the Substrate Used in TEM Analysis

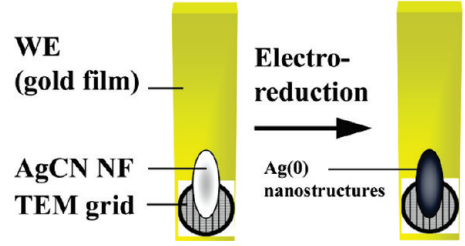

The same experimental procedure was used for the electrochemical reduction of $Cu(OH)_2$ NFs. $Cu(OH)_2$ NFs were drop-cast from a dichloromethane solution onto the Au/glass/Au junctions and were electrolyzed for 1 h at −1.65 V.

The stability of the fibers in 0.1 M $KClO_4$ was verified via SEM imaging [AgCN−SMA NF (20 min), and $Cu(OH)_2$ NF (60 min)]. AgCN−SMA NFs were very stable. Small areas of the $Cu(OH)_2$ NF network appeared to be damaged after 1 h, probably because of a recrystallization process of $Cu(OH)_2$ into CuO.

2.7. TEM Characterization of the Reduced Ag^0 Nanostructures. AgCN−SMA NFs were drop-cast onto a Au TEM grid placed over a Au-coated glass slide (Scheme 2). The TEM grid was mechanically attached to the substrate by the fibers. After electrochemical reduction, the substrate was rinsed in Milli-Q water, and the TEM grid was gently detached to perform the TEM imaging.

3. RESULTS AND DISCUSSION

3.1. Electrochemical Study of a AgCN−SMA NF Network. Van de Ven and we recently developed a simple, reproducible, high-yield, high-scale (>100 mg), and inexpensive route to producing silver(I) cyanide (AgCN) NFs (13). This technique takes advantage of SMA self-assembly to form polymeric nanotubes (52, 53), which guides AgCN growth into very high aspect ratio (500−10 000) NFs. The resulting NFs aggregate into stable dense, millimeter-scale networks. Two types of fibers are produced (Figure 1).

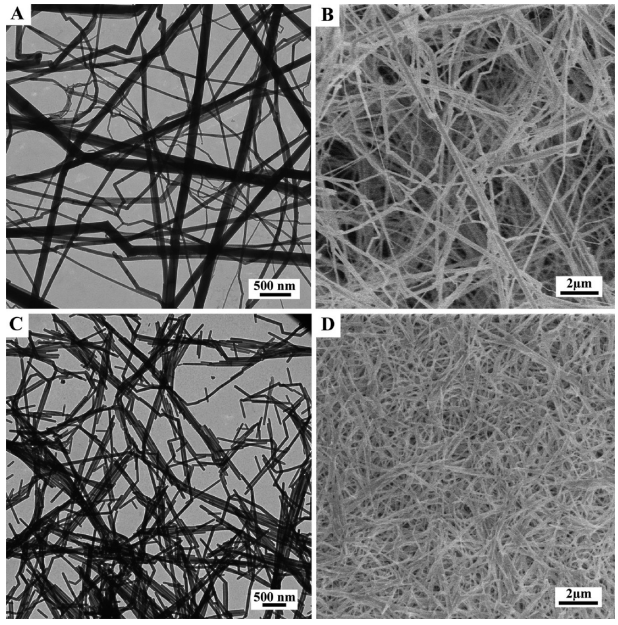

FIGURE 1. Electron microscopy images of the AgCN fibers. TEM (A) and SEM (B) images of AgCN−SMA_{NaBH_3CN} NFs. TEM (C) and SEM (D) images of AgCN−SMA_{NaCN} NFs.

Polydisperse and extremely long AgCN NFs (5−200 nm wide and >50 μm long) are synthesized by the reduction of $AgNO_3$ with $NaBH_3CN$ in the presence of SMA nanotubes (termed AgCN−SMA_{NaBH_3CN}). Very large bundles of fibers (diameter up to 500 nm) are observed. Shorter and highly monodisperse (65 ± 9 nm wide) AgCN NFs result from precipitation of NaCN and $AgNO_3$ in the presence of SMA nanotubes (termed AgCN−SMA_{NaCN}). An electrochemical study of these fibers (Figure 2) and their transformation into metallic silver nanostructures was undertaken. Because AgCN is an insoluble salt in neutral water (AgCN solubility product: $K_{sp} = 5.97 \times 10^{-17}$) (54), AgCN−SMA NF is considered to be a solid species.

Electrochemical examination of pure insoluble AgCN(s) crystals and water-soluble pure $KAg(CN)_2$ (see the Supporting Information, SI) reveals that these two native forms of silver cyanide and the AgCN−SMA NFs have similar cyclic voltammograms (Figures S1−S6 in the SI).

The absence of a significant quantity of native metallic Ag in AgCN and the AgCN−SMA fibers was verified by CV. Typically, less than 0.01 % of native Ag^0 was detected by CV at the beginning of the experiments. Upon scanning cathodically from 0 to −0.9 V, a reduction wave A_1 appears at potentials (V) below −0.40 V, with approximately $E_{red1} = -0.65$ V. A_1 corresponds to the reduction of AgCN to metallic Ag (eq 1).

$$AgCN(s) + e^- \rightarrow Ag^0 + CN^- \qquad (1)$$

This is in agreement with previous work in which the reduction of $Ag(CN)_2^-$ begins at similar potentials on a Ag electrode in a neutral aqueous solution (0.1 M $NaClO_4$) (50). The electroreduction of $Ag(CN)_2^-$ on Ag has been postulated to proceed via the reduction of adsorbed AgCN(s), generated

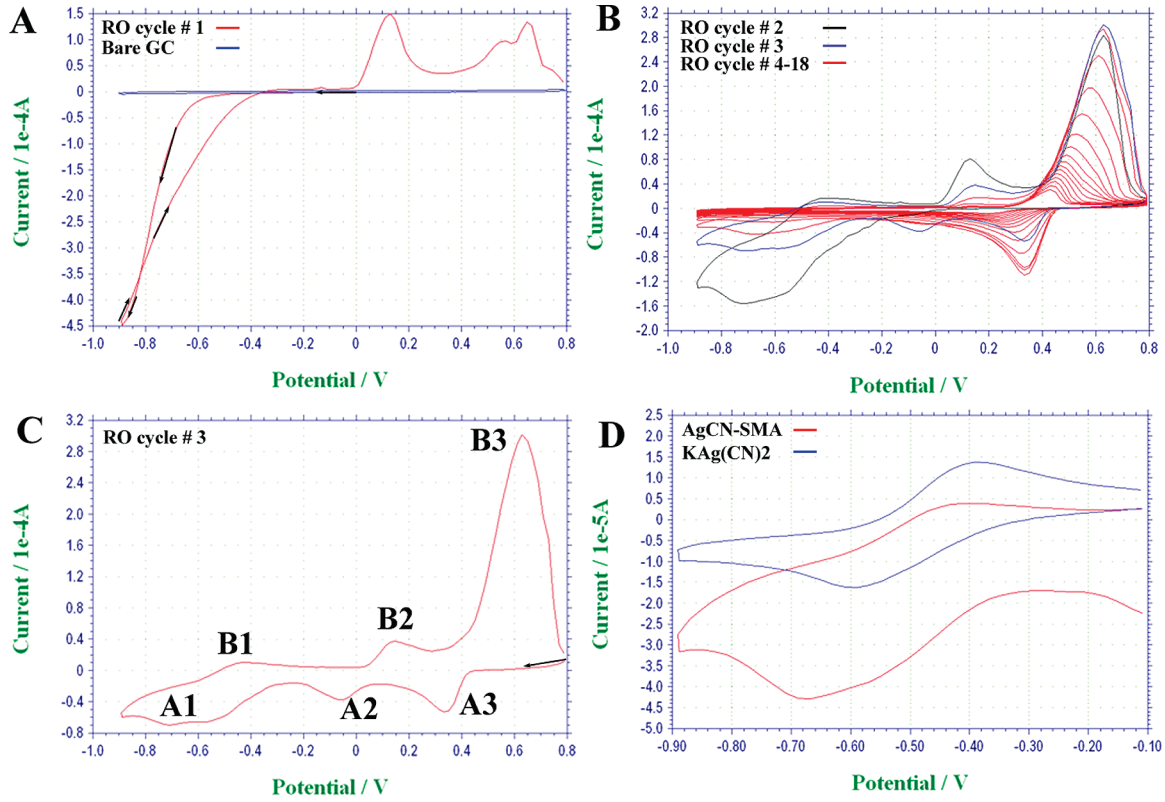

FIGURE 2. CV of AgCN−SMA_{NaCN} NFs deposited on a GC electrode in 0.1 M $KClO_4$ (scan rate: 200 mV · s^{-1}). (A) Blue curve: bare GC. Red curve: initial reduction−oxidation (RO) cycle, following the sequence of 0 to −0.9 to +0.8 V. (B) Subsequent RO cycles (2nd to 18th). (C) 3rd RO cycle (starting from +0.8 V). (D) Region of AgCN reduction. Blue curve (top): soluble salt $KAg(CN)_2$ [10 mM $KAg(CN)_2$ in 0.1 M $KClO_4$ on a GC electrode]. Red curve (bottom): AgCN−SMA_{NaCN}.

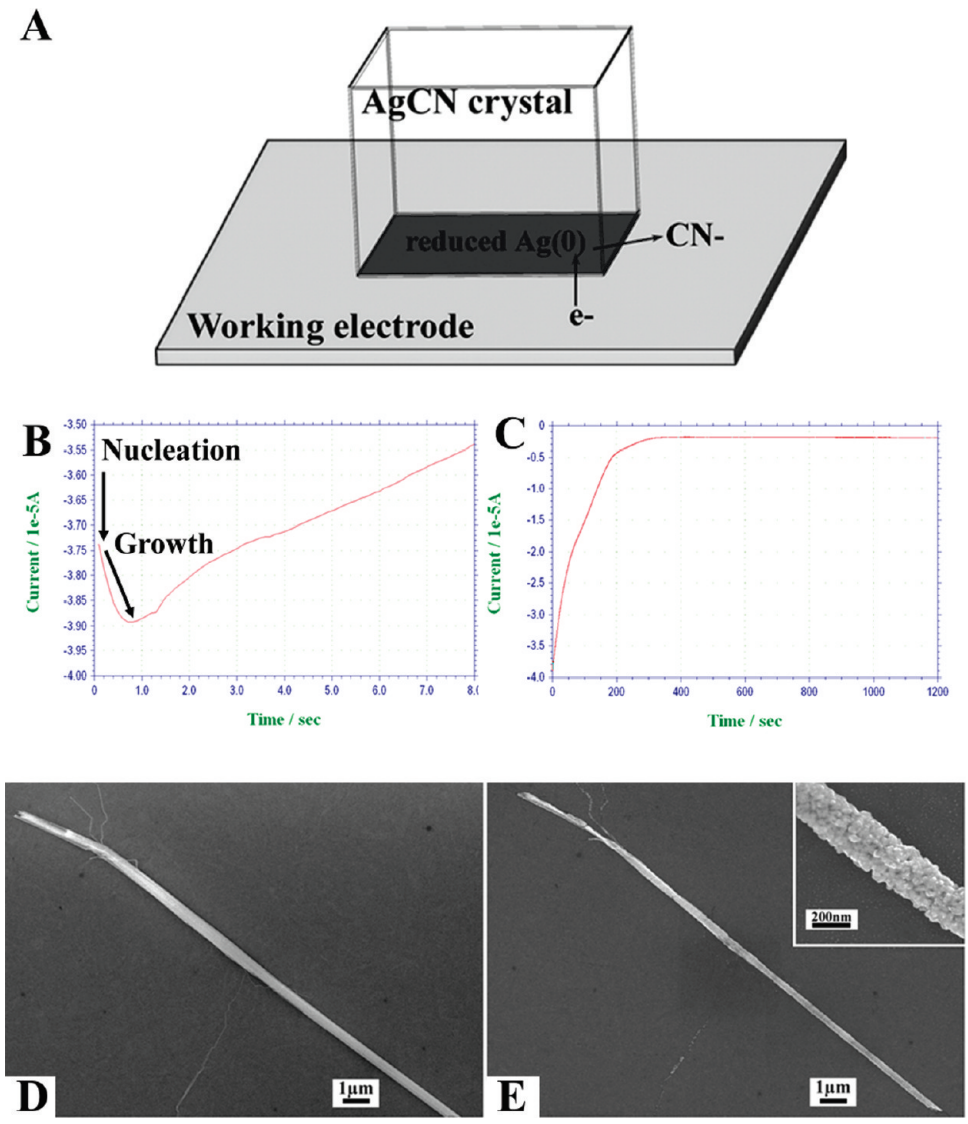

FIGURE 3. (A) Schematic of the electrochemical reduction of solid AgCN via the injection of electrons and the release of CN^- at the electrode/AgCN/electrolyte interface. (B) Early stages of the electrochemical reduction of AgCN−SMA_{NaCN} NFs on a graphite electrode (−0.55 V for 1200 s). Nucleation-and-growth processes characteristic of the electrochemical conversion of solid species are observed. (C) Complete i−t curve. (D and E) SEM images of isolated AgCN−SMA_{NaBH_3CN} NFs before (D) and after (E) reduction at −0.6 V on HOPG. The inset in E is a higher magnification image of the reduced NF. It is evident from these images that both the position and shape of the isolated fibers are preserved during the electrochemical reduction.

by decomplexation of $Ag(CN)_2^-$. Upon cycling from −0.9 to +0.8 V, a broad anodic wave B_1 corresponding to the oxidation of Ag^0 to silver cyanide appears at $V > -0.55$ V, with $E_{ox1} = -0.5$ V (eq 2).

$$Ag^0 + xCN^- \rightarrow Ag(CN)_x^{1-x} + e^- \qquad (2)$$

Ag is known to form various $Ag(CN)_x^{1-x}$ ions depending on the relative concentration of Ag^+ and CN^- (55). A mixture of AgCN(s) and $Ag(CN)_x^{1-x}$ ions is expected to form during the oxidation wave B_1 because of the CN^- gradient generated (as per eq 1) in the vicinity of the electrode. As the scan moves to more anodic potentials, two oxidation waves, B_2 and B_3, appear. These originate from the oxidation of CN^- and Ag^0, respectively. The assignment of A_2 and B_2 is somewhat uncertain given the rather incomplete understanding of the silver cyanide system in neutral aqueous media (see the SI). It is beyond the scope of this work to determine the complex electrochemistry of these metal cyanides. B_2 is, however, tentatively assigned to the formation of $(CN)_2$ (56), via formation of a cyano radical (eqs 3 and 4 and the SI).

$$CN^- \rightarrow CN^\bullet + e^- \qquad (3)$$

$$2CN^\bullet \rightarrow (CN)_2 \qquad (4)$$

The third oxidation wave, B_3, is dominated by the oxidation of metallic Ag to Ag^+ (eq 5) (57).

$$Ag^0 \rightarrow Ag^+ + e^- \qquad (5)$$

During the second reductive scan (+0.9 to −0.8 V), two reduction waves, A_2 and A_3, are observed, corresponding to the reduction of the species generated by B_2 and B_3. A_3 is assigned to the reduction of Ag^+ (eq 6), and A_2 is assigned to the reduction of $(CN)_2$ to CN^- (eq 7).

$$Ag^+ + e^- \rightarrow Ag^0 \quad (6)$$

$$(CN)_2 + 2e^- \rightarrow 2CN^- \quad (7)$$

3.2. Electrochemical Conversion of AgCN−SMA NFs into Ag^0 Nanostructures (Nanoprisms, NPs, and NFs). The electrochemical reduction of AgCN−SMA NFs that have been drop-cast onto graphite, HOPG, Au, and Pt electrodes was studied. Under constant potential electrolysis conditions, the current−time profile of the reduction is consistent with a nucleation-and-growth process and is fundamentally different from the monotonic decrease of the current in diffusion-limited reactions. Because the AgCN−SMA NFs are successively reduced to metallic silver, the active surface area of the WE and the amount of AgCN electrically connected to the potentiostat increases, leading to a characteristic increase in the current. After a given electrolysis time, which depends on the quantity of material deposited on the electrode, the quantity of AgCN available to be reduced decreases as noted by the decrease in the measured current. At HOPG, for $V_r \leq -0.6$ V, the position and shape of isolated NF is preserved, consistent with a solid−solid transformation of the AgCN fibers into Ag^0 fibers with similar geometries (Figure 3). However, the reduction of dense networks of fibers produces different structures. The following sections present the electrochemical reduction of AgCN NF networks at Au/glass/Au junctions, with a glass domain width varying between 150 and 300 μm (cf. Scheme 1). The morphology and dimensions of the reduced NF were altered by changing V_r and the nature of the supporting substrate (conductive vs insulating).

3.2.1. Ag^0 Nanostructures Produced at the Au Electrode. A range of Ag^0 nanostructure geometries is produced on Au as a function of V_r (Figure 4). At $V_r = -0.3$ V, the reduction of the AgCN−SMA_{NaCN} NF networks located on the Au electrode forms a continuous layer of fused and large Ag^0 NPs. A small number of nanoprisms are observed. The reduction is very slow and incomplete. At $V_r = -0.4$ and -0.45 V, large Ag^0 nanoprisms are formed along with large Ag^0 NPs (approximate width of the prism diagonal: 1250 ± 540 nm at −0.4 V). At $V_r = -0.55$ V, coalescence of the AgCN−SMA_{NaCN} fibers into Ag^0 nanoprisms with a predominant hexagonal shape (approximate width of the hexagon diagonal: 300 ± 100 nm) occurs in high yield (Figure 4). The dependence of the material formed on V_r is striking: at $V_r = -0.6$ V, the number density of the prisms formed decreases drastically, and at $V_r \leq -0.65$ V, they no longer form. Fusion of the nanostructures is more pronounced at $V_r \leq -0.65$ V. In some rare cases, a fibrous geometry of the networks is observed (as seen in Figure 4, at $V_r = -0.65$ V).

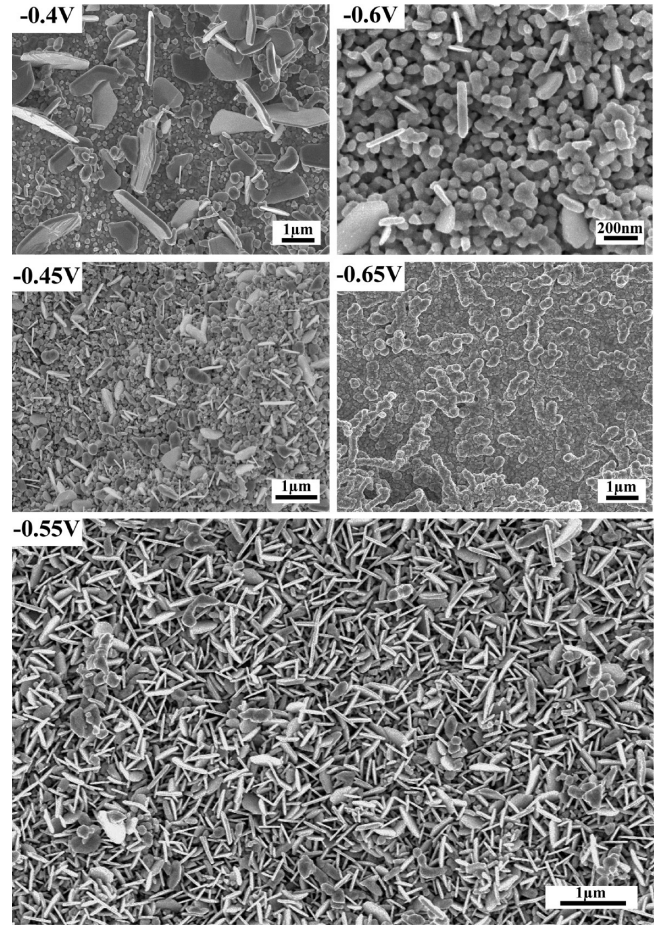

FIGURE 4. SEM images showing the different typical morphologies of the Ag^0 nanostructures formed at a Au electrode via the reduction of AgCN−SMA_{NaCN} at different V_r values in 0.1 M $KClO_4$. A small quantity of unreduced fibers can be seen in the SEM image of the sample reduced at −0.4 V.

3.2.2. Ag^0 Nanostructures Produced over the Glass Junction. The effect of V_r on the resulting nanostructures, when produced over the insulating glass substrate, was also studied. A strong dependence of V_r on both the size and morphology of the reduced AgCN−SMA fibers is observed (Figure 5). At modest V_r values (−0.3 V), the reduction is extremely slow and the nanostructures formed are not homogeneous. When V_r is decreased to −0.4 and −0.45 V, a mixture of large NPs (diameters of 125 and 135 nm, respectively) and large nanoprisms (750 and 500 nm wide, respectively) is produced. At −0.5 V, the original shape of the network is visible. Large fibers (190 nm in diameter) formed from aggregated NPs (85 nm in diameter) are observed. At −0.55 and −0.6 V, NPs are no longer distinguishable from the fibers, and their sizes decrease (115 and 90 nm wide at −0.55 and −0.6 V, respectively). When the potential is decreased below −0.6 V, the fibers fuse, leading to larger fibers (105 nm wide at −0.65 V, 170 nm at −0.8 V, and 240 nm at −0.9 V). Although we do not have a definitive explanation for the differences in the morphology and size obtained as a function of V_r, we anticipate that kinetic effects play an important role in these effects (vide infra). When the driving force is low ($V_r > -0.55$ V), nucleation and crystallization of Ag^0 into NPs and nanoprisms are

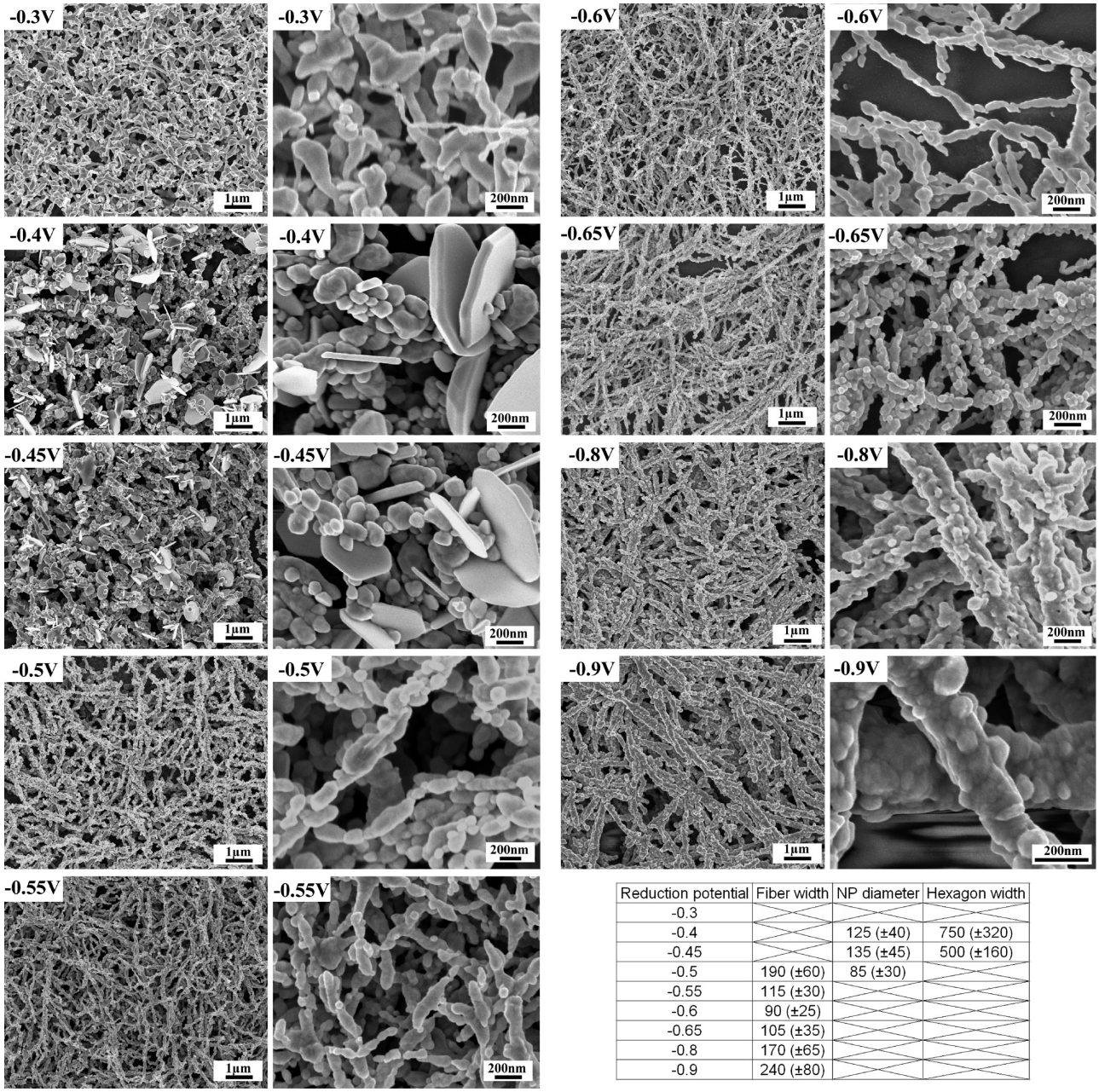

Reduction potential	Fiber width	NP diameter	Hexagon width
-0.3			
-0.4		125 (±40)	750 (±320)
-0.45		135 (±45)	500 (±160)
-0.5	190 (±60)	85 (±30)	
-0.55	115 (±30)		
-0.6	90 (±25)		
-0.65	105 (±35)		
-0.8	170 (±65)		
-0.9	240 (±80)		

FIGURE 5. SEM images showing the different morphologies of the Ag^0 nanostructures formed on the glass substrate via the reduction of AgCN−SMA_{NaCN} NFs on Au/glass/Au junctions as a function of V_r in 0.1 M $KClO_4$. Bottom right: average sizes (in nm) of the Ag^0 nanostructures produced as a function of V_r (statistics derived from at least 150 measurements).

favored. When V_r is <−0.55 V, the reduction is fast and continuous along the fibers. At highly cathodic potentials ($V_r \leq -0.55$ V), the reduction is so fast that significant fusion of the fibers occurs. The strain induced by the physical transformation of AgCN into Ag^0 might be too high, while the fibers are electrochemically reduced at multiple points, leading to fused large fibers.

3.2.3. Influence of the Initial AgCN−SMA NF Size on the Ag^0 Nanostructures Formed. The influence of the initial AgCN NF size on the resulting Ag^0 nanostructures was examined by using large AgCN−SMA_{NaBH_3CN} NFs (13). As expected, the electrochemical reduction of these fibers leads to longer and wider fibers. At −0.55 V, a mixture of Ag^0 nanoprisms and NFs is produced from the AgCN NF. At −0.65 V, large fibers made of aggregated NPs are formed over the glass substrate (Figure 6). The size of the Ag^0 nanostructures produced is not as reproducible as that in the AgCN−SMA_{NaCN} NF case. We attribute this to the inhomogeneity of the initial AgCN−SMA_{NaBH_3CN} NF fibers and their networks, which differ from the highly monodisperse AgCN−SMA_{NaCN} NFs that form dense and homogeneous networks. At −0.8 V, similar fibers are obtained, although a significant fusion of the NPs within the fibers is seen.

3.3. Characterization of the Electrosynthesized Materials. The complete reduction of AgCN to Ag^0 is verified by EDS and electron diffraction (Figure 7). EDS analysis reveals the absence of Au on the Ag^0 structures produced over the glass surface, ruling out any possible

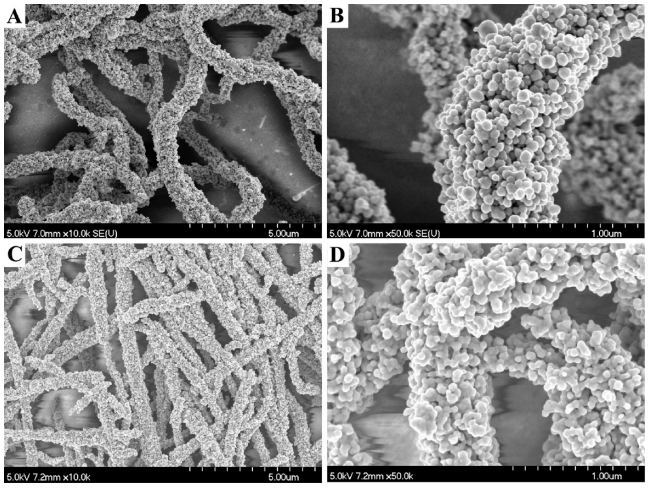

FIGURE 6. SEM images of AgCN−SMA_{NaBH_3CN} NFs reduced over the glass surface at −0.65 V (A and B) and −0.8 V (C and D). Electrolysis time = 20 min.

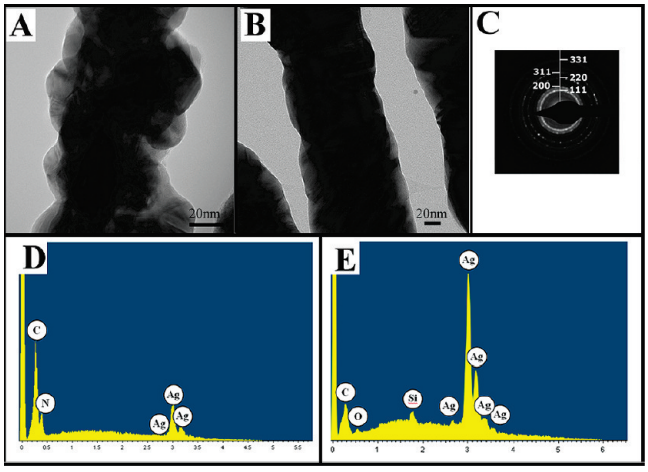

FIGURE 7. (A and B) TEM images of AgCN−SMA_{NaCN} NFs reduced on a Au TEM grid for 20 min (A, $V_r = -0.55$ V; B, $V_r = -0.65$ V). (C) Typical electron diffraction pattern of the Ag^0 nanostructures produced on the Au TEM grid, consistent with them being Ag^0. (D) EDS spectrum of a pure AgCN−SMA_{NaCN} NF on silicon. (E) Typical EDS spectrum of the Ag^0 nanostructures produced over the glass substrate, clearly showing the absence of N and Au, which could originate from CN^- and the Au electrode. The remaining peak at ≈0.25 keV in the EDS spectrum is attributed to both Au and environmental C. This peak has previously been reported in the EDS spectrum of a Ag standard (99.99% purity) (58). Both EDS spectra were acquired in an SEM environment.

electrochemical oxidation and redeposition of Au onto the reduced materials. TEM analysis of the products was conducted by drop-casting the AgCN−SMA NF on a gold TEM grid placed over a Au-coated glass slide (see the Experimental Section). During the electrochemical reduction, the reduced fibers electrically connect the TEM grid to the WE. This result suggests a form of electrochemical welding, with the AgCN fibers acting as a cold solder.

3.4. Propagation of the Metallic Boundary. Because AgCN is neither a good ionic conductor nor an electronic conductor, the reduction process occurs at the electrode/AgCN NF/electrolyte interface. The reduced AgCN−SMA wires act as an extension of the WE, reducing silver cyanide, which is in close proximity. The propagation of this interface was monitored via SEM, and the connection between AgCN and Ag^0 is clearly identifiable for all morphologies observed, on both the Au and glass substrates (Figure 8). The fibers located on the Au electrode connected to the WE are the first to be reduced. Once most of them are reduced, the "reduction front" creeps over the glass zone. This propagation is visible to the naked eye as a change in the color of the fibers during reduction (going from white to black/silvery and moving in the direction of the Au film to the glass area).

As described above, the structures produced on the Au electrode and over the insulating glass junction are different. SEM imaging clearly shows this change in morphology occurring at the Au/glass junction (Figure 9).

3.5. Discussion. The origin of the difference between the structures formed on the Au film and on the glass is initially puzzling. Upon application of a reducing potential, multiple nucleation events simultaneously occur on the fibers in contact with the Au electrode, producing a high density of Ag^0 nuclei (cf. Scheme 3). As the reduction proceeds, these nuclei grow into larger structures up to a critical point where they coalesce. At sufficiently negative V_r (≤ -0.65 V), the reduction is fast, producing disorganized aggregated structures on the Au surface. As AgCN is reduced, the CN^- ions thus released diffuse away from the electrode and the fibers. At the Au electrode, because nucleation of Ag^0 occurs everywhere, the cyanide gradient around the NFs is much greater than that around the NFs formed on the glass. This is because, in the glass case, CN^- is released only at the extremity of the Ag^0 structures (cf. Scheme 3). The AgCN fibers might be partially dissolved when the concentration of CN^- generated is high enough, forming the soluble $Ag(CN)_x^{1-x}$ ions in the vicinity of the electrode. This partial dissolution along with the reduction of the $Ag(CN)_x^{1-x}$ ions could be the origin of the featureless structures obtained at highly negative potentials on Au.

However, when the reduction boundary reaches the Au/glass junction, the growth is spatially constrained at this interface, and it becomes unidirectional. This restriction of the reduction conditions limits the concentration of CN^- generated as well as the physical fusion of the fibers. At −0.55 V, the change in the morphology is very sharp. On Au, homogeneous Ag^0 nanoprisms are formed, while on glass, fused fibers are obtained.

Ag nanoprisms are of great interest because of their intense light-scattering properties through surface plasmon excitation (59, 60). They are especially well-known for their high sensitivity toward small changes in the dielectric constant of their surroundings through large shifts of their local surface plasmon resonance (SPR) (61, 62). By changing their size, one can tune their SPR from the visible to the IR range (60). The first reliable and high-yield synthesis of Ag nanoprisms was based on the photochemical growth of Ag on small Ag NP seeds (59). Various methods have been used since, including photochemical and radiolysis syntheses, biological thermal syntheses, microwave- and ultrasound-assisted techniques, and wet-chemical syntheses with the absence of light (60). However, all of these methods require

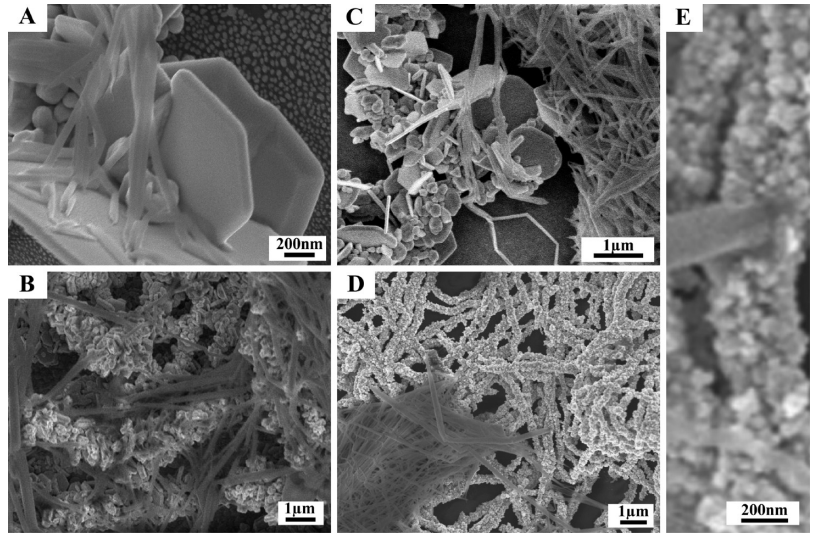

FIGURE 8. SEM images showing the boundary between the AgCN NF and the Ag^0 NF. On Au: (A) $AgCN-SMA_{NaCN}$ NF reduced at −0.4 V; (B) $AgCN-SMA_{NaBH_3CN}$ NF reduced at −0.55 V. On glass: (C) $AgCN-SMA_{NaCN}$ NF reduced at −0.4 V; (D) $AgCN-SMA_{NaBH_3CN}$ NF reduced at −0.8 V. (E) 10× zoom image of part D showing the junction between one unreduced AgCN fiber (appearing smooth) and the reduced Ag^0 network (appearing as a collection of NPs).

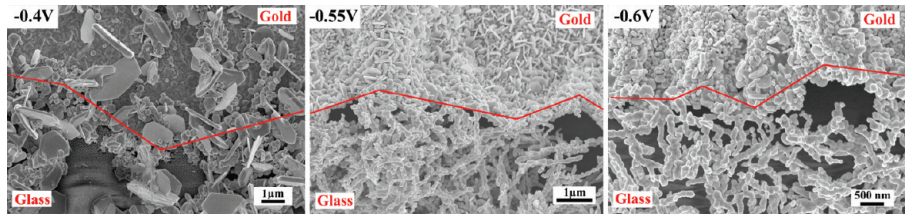

FIGURE 9. SEM images of the Au/glass junction showing the differences in morphology of the Ag^0 structures produced by the reduction of $AgCN-SMA_{NaCN}$ NFs. The Au area is located on the top half of the images, while the glass is on the bottom half of the images. The red line represents the physical boundary between the gold and the glass areas. At −0.55 V, the sharp change from fibers to nanoprisms upon moving through the Au/glass junction is especially striking.

the initial fabrication of small Ag NPs (2−6 nm in diameter) used as seeds to direct the subsequent growth of the nanoprisms. It is generally accepted that the preferential growth of platelike Ag nanostructures is ruled by kinetic and crystallographic factors (60, 63). The use of weak reducing agents such as ascorbic acid is of particular importance because it allows for the slow growth of prisms onto the Ag seeds. Fast isotropic growth of the Ag NPs into larger particles, on the other hand, occurs when a stronger reducing agent such as $NaBH_4$ is used (63). The capping of specific crystallographic faces by surfactants or anions present during the synthesis has also been found to play an important role in the 2D growth of nanoprisms (60).

Ag^0 nanoprisms form in high yield upon the electrochemical reduction of large networks (>50 μm wide) of $AgCN-SMA_{NaCN}$ NFs at −0.55 V on Au (Figure 4) and Pt electrodes (Figure 10). They also form on graphite, but with lesser densities (Figure S7 in the SI). To investigate the influence of the solid nature of these fibers, we conducted the electroreduction of the soluble silver cyanide salt, $KAg(CN)_2$, onto Pt electrodes (Figure 11). The experiments were performed in both basic (0.01 M NaOH) and neutral conditions (0.1 M $KClO_4$). At basic pH, nucleation of Ag NPs occurs at the defect sites of the Pt electrode along with the formation of nanoprisms. At neutral pH (0.1 M $KClO_4$), only Ag NPs are formed.

Because the wet-chemical synthesis of Ag nanoprisms is not well understood, we do not have as yet a clear explanation for their formation during the electrochemical reduction of AgCN−SMA NFs and $KAg(CN)_2$. However, as discussed above, the slow reduction due to the modest reducing potential used and the presence of cyanide anions that strongly coordinate with Ag are expected to play an important role in their formation. The pH dependence of the Ag nanoprism synthesis via the electroreduction of $KAg(CN)_2$ suggests that a basic pH favors their formation from the reduction of solid AgCN fibers. A local pH increase due to the release of free CN^- ions during the reduction of AgCN−SMA NFs (HCN pK_a = 9.21) (54) could play a role in determining the geometry of the Ag^0 nanostructures produced, given that the pH can influence the formation of Ag nanoprisms (60, 64).

SEM images (Figure 8) clearly verify the physical connection of the nonreduced AgCN−SMA fibers with the Ag^0 structures. This supports the fact that the NF network acts as a finite source of Ag^+ and CN^- ions, localized and immobilized at the electrode surface, providing a constant and slow feed of ions that are reduced on the sides of the Ag^0 nanoprisms. The Ag^0 nuclei formed at the early stages of the reaction are seeds for the nanoprism growth, in a very similar manner to the use of small Ag NPs as seeds in the wet-chemical syntheses of Ag^0 nanoprisms (60). The differ-

Scheme 3. Influence of the Reduction Potential V_r on the Geometry of the Ag^0 Nanostructures Produced by the Electrochemical Reduction of AgCN−SMA_{NaCN} NFs[a]

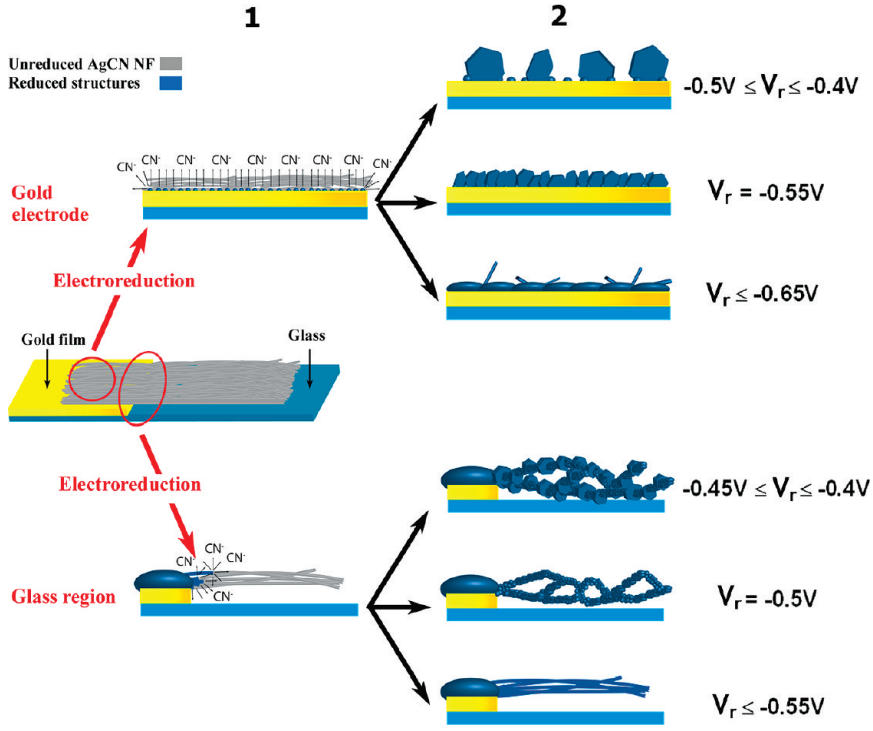

[a] The first half of the Au/glass/Au junction is shown for clarity. The differences in nucleation (1) due to the location of the fibers (on Au or on glass) are presented, along with the various morphologies produced when the reduction is complete (2).

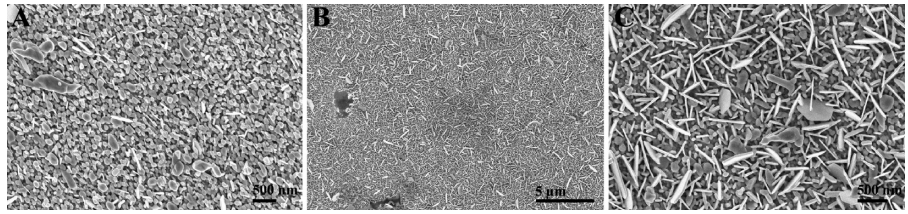

FIGURE 10. SEM images of the Ag^0 nanoprisms formed upon reduction of an AgCN−SMA_{NaCN} NF network on a Pt electrode at −0.55 V for 20 min in 0.1 M $KClO_4$: (A) SEM image representative of the structures formed at the periphery of the nanoprism film; (B and C) low- and high-magnification SEM images of the Ag^0 nanoprism film.

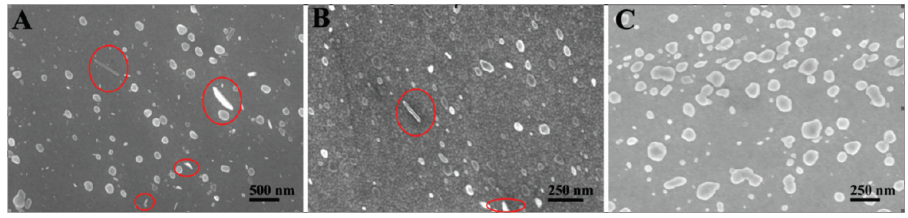

FIGURE 11. Ag NPs and nanoprisms made via the electroreduction of 1 mM $KAg(CN)_2$ on a Pt electrode: (A) in 0.01 M NaOH at −0.45 V (1200 s); (B) in 0.01 M NaOH at −0.55 V (250 s); (C) in 0.1 M $KClO_4$ at −0.55 V (500 s).

ence in the size and density of Ag^0 nanoprisms produced at −0.4 and −0.55 V is likely to be due to the difference in the density of nuclei produced because the number of nuclei generated depends on V_r. At a modest reducing potential, a low density of Ag^0 nuclei are produced, while at higher overpotentials (i.e., higher reducing potential), a higher density of Ag^0 nuclei are produced (37). For simplicity, we assume that the local coverage of AgCN−SMA_{NaCN} NFs is similar (on the micrometer scale) in all of our experiments, implying a similar local concentration of Ag^+ species. It follows that, after complete reduction, a low density of seeds (obtained via a low reducing potential, $V_r = -0.4$ V) will lead to large Ag^0 nanostructures, while a higher density of nuclei (obtained with a higher reducing potential, $V_r = -0.55$ V) will lead to smaller Ag^0 nanostructures because of the faster depletion of Ag^+ ions as the reduction proceeds. This indeed is observed, whereas at −0.4 V, a low density of large nanoprisms (average width: 1250 ± 540 nm) is observed. At −0.55 V, dense films of smaller nanoprisms (average width: 300 ± 100 nm) are observed.

Interestingly, the preferential orientation of the nanoprisms is tilted from the normal of the substrate surface. It

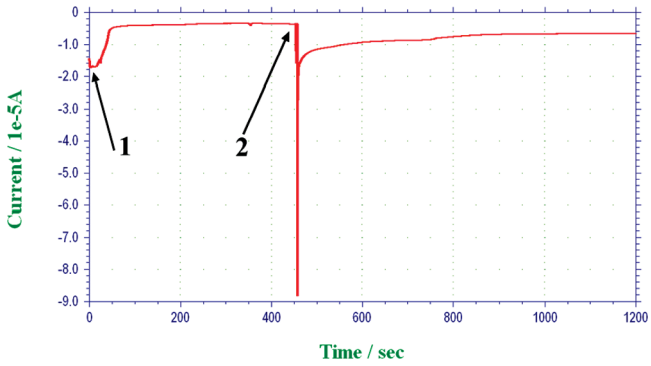

FIGURE 12. Typical $i-t$ curve obtained during the electrochemical reduction of Au/AgCN−SMA fibers/Au junctions (fibers, AgCN−SMA_{NaCN} NF; reduction conditions, $V_r = -0.55$ V, 20 min). Arrow 1: nucleation and propagation of the reduction of the NF present on the first Au pad and over the glass. Arrow 2: Ag^0/AgCN boundary reaching the second Au conductive pad.

has been reported that Ag^0 nanoprisms grow in solution along the hexagon edges (i.e., ⟨111⟩ and ⟨100⟩ direction) but not along their thickness axis (60, 63, 65). Because Au, Ag, and Pt have the same face-centered-cubic crystal structure with similar lattice parameters ($a_{Ag} = 4.0862$ Å, $a_{Au} = 4.0786$ Å, and $a_{Pt} = 3.9231$ Å) (54, 66), it is likely that the Ag^0 nanoprisms nucleate and grow epitaxially along the ⟨111⟩ or ⟨100⟩ direction of the Au and Pt crystallites. However, the fact that Ag^0 nanoprisms also form on graphite rules out the nature and orientation of the substrate being the main cause of their formation.

It is intriguing that, at $V_r = -0.4$ and -0.45 V, NFs made of Ag^0 NPs and nanoprisms are observed over the glass substrate, while fibrous aggregation of NFs is seen at $V_r = -0.55$ V, (Figure 5). In these cases, because the nanoprisms produced are significantly larger than the ones formed at $V_r = -0.55$ V, we speculate that the reduction slowness is the determining force for the formation of these large Ag^0 nanoprisms.

Although the electrochemical synthesis of metallic NPs has previously been reported (19, 20), this is, to our knowledge, the first demonstration of the electrochemical synthesis of metallic nanoprisms. This fabrication technique does not require any templating agents or any surfactant, which should simplify the understanding of the processes in play during their formation.

4. ELECTRICAL CHARACTERIZATION OF THE AU/AG^0 NANOSTRUCTURES/AU JUNCTIONS

We investigated metallic contact formation through the electrochemical reduction of the Au/AgCN−SMA NF/Au junctions. The current-time curve (Figure 12) shows the features expected of a nucleation-and-growth process. Once the metal boundary reaches the other side of the junction, the area of contact between the unreduced fibers and the conductive part of the junction dramatically increases because the whole Au pad is now connected to the potentiostat. This is apparent in a second increase in the current due to a new nucleation-and-growth process, caused by the Faradaic current, and to the capacitive current (the capacitive current decay is clearly seen in this case). The absence of electrical conduction was verified prior to the experiment. *IV* curves show that an excellent electrical contact has been formed between the two Au electrodes after formation of the Ag^0 junctions (Figure 13). For example, the conductance of the pure Au film measured over 1 cm was 0.8 S, while the Au/Ag^0 NF/Au junction produced via the electrochemical reduction of AgCN−SMA_{NaBH_3CN} (−0.8 V for 20 min) exhibits a conductance of 0.5 S over 1 cm.

Precise alignment and positioning of nanowires using alternating-current electric fields or Langmuir−Blodgett films have been reported in recent years (67−69). Coupling these methods with our technique could allow for parallel patterning of metallic nanowires with excellent electrical connections.

5. $CU(OH)_2$ NFS

We recently reported the interfacial three-dimensional assembly of $Cu(OH)_2$ NFs into porous spheres using a water-in-oil microemulsion (41). A rapid synthesis of 15-nm-wide $Cu(OH)_2$ NF results (see the Experimental Section). CV of these fibers drop-cast onto a GC electrode (Figure 14) is consistent with them being composed of only $Cu(OH)_2$ (70).

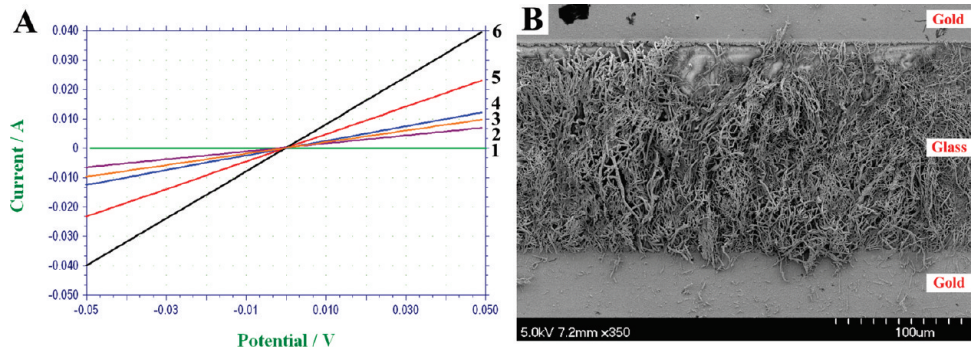

FIGURE 13. (A) *IV* curves of a number of Au/Ag^0 NF/Au junctions. The electrodes were separated by ca. 1 cm. Curves: 1 (green), typical *IV* curve of the junction prior to reduction; 2 (purple), AgCN−SMA_{NaCN} NF reduced 20 min at −0.6 V; 3 (orange), AgCN−SMA_{NaBH_3CN} NF reduced 20 min at −0.65 V; 4 (blue), AgCN−SMA_{NaBH_3CN} NF reduced 20 min at −0.55 V; 5 (red), AgCN−SMA_{NaBH_3CN} NF reduced 20 min at −0.8 V. Curve 6 (black) is a typical *IV* curve of the Au electrode measured in an identical configuration. (B) Large-scale SEM image of an Au/AgCN-SMA_{NaBH_3CN}/Au junction after electrochemical reduction (20 min at −0.8 V). Scale bar: the distance between 2 white markers is 10 μm (the whole scale bar represents 100 μm).

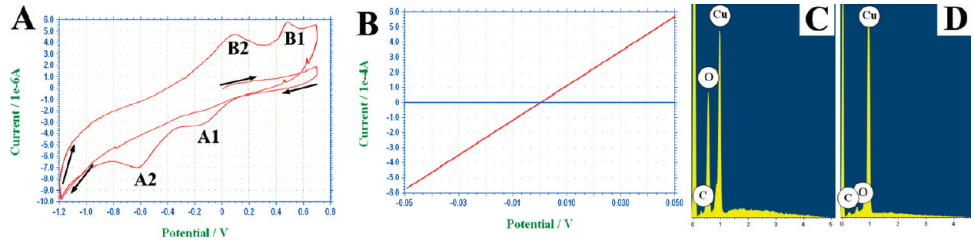

FIGURE 14. (A) CV of $Cu(OH)_2$ NFs deposited onto GC 0.1 M $KClO_4$ (scan rate: 100 mV · s^{-1}). The first cycle (black arrows) shows the overpotential needed to initiate the electroreduction of $Cu(OH)_2$. (B) *IV* curves of the Au/$Cu(OH)_2$ NF/Au junction before (blue curve) and after (red curve) electrochemical reduction (1 h at −1.65 V). Good conductivity of the junction is observed after reduction. The EDS spectra of the $Cu(OH)_2$ NF before (C) and after reduction (D) confirm the purity of the as-synthesized $Cu(OH)_2$ fibers. The complete reduction of $Cu(OH)_2$ into Cu^0 is evident by the large decrease of the O Kα line at 0.532 keV after reduction. We expect the residual O signal to be due to the native oxide layer formed after exposing the Cu^0 nanostructures to air.

The cathodic wave A_1 corresponds to the reduction of $Cu(OH)_2$ to Cu_2O (eq 8) (70).

$$2Cu(OH)_2 + 2e^- \rightarrow Cu_2O + H_2O + 2OH^- \quad (8)$$

The cathodic wave A_2 corresponds to the reduction of Cu_2O and $Cu(OH)_2$ to Cu^0 (eqs 9 and 10) (70).

$$Cu(OH)_2 + 2e^- \rightarrow Cu + 2OH^- \quad (9)$$

$$Cu_2O + H_2O + 2e^- \rightarrow 2Cu + 2OH^- \quad (10)$$

Cu^0 generated by A_2 is oxidized at B_1 and B_2. The local pH in the vicinity of the electrode is unknown but should be >7 because of the release of OH^- during the reduction of $Cu(OH)_2$. Because copper readily forms oxides in neutral H_2O (71), the different reactions that can take place are described by eqs 11−15 (70). The formation of Cu_2O, CuO, and $Cu(OH)_2$ is expected to arise from the oxidation waves B_1 and B_2.

$$2Cu + 2OH^- \rightarrow Cu_2O + H_2O + 2e^- \quad (11)$$

$$Cu + 2OH^- \rightarrow CuO + H_2O + 2e^- \quad (12)$$

$$Cu_2O + 2OH^- \rightarrow 2CuO + H_2O + 2e^- \quad (13)$$

$$Cu + 2OH^- \rightarrow Cu(OH)_2 + 2e^- \quad (14)$$

$$Cu_2O + H_2O + 2OH^- \rightarrow 2Cu(OH)_2 + 2e^- \quad (15)$$

Electrolysis at −1.65 V of the $Cu(OH)_2$ NFs on Au/glass/Au junctions leads to dense, porous networks of conductive monodisperse Cu^0 short NFs (33 ± 11 nm wide), as seen in Figure 15.

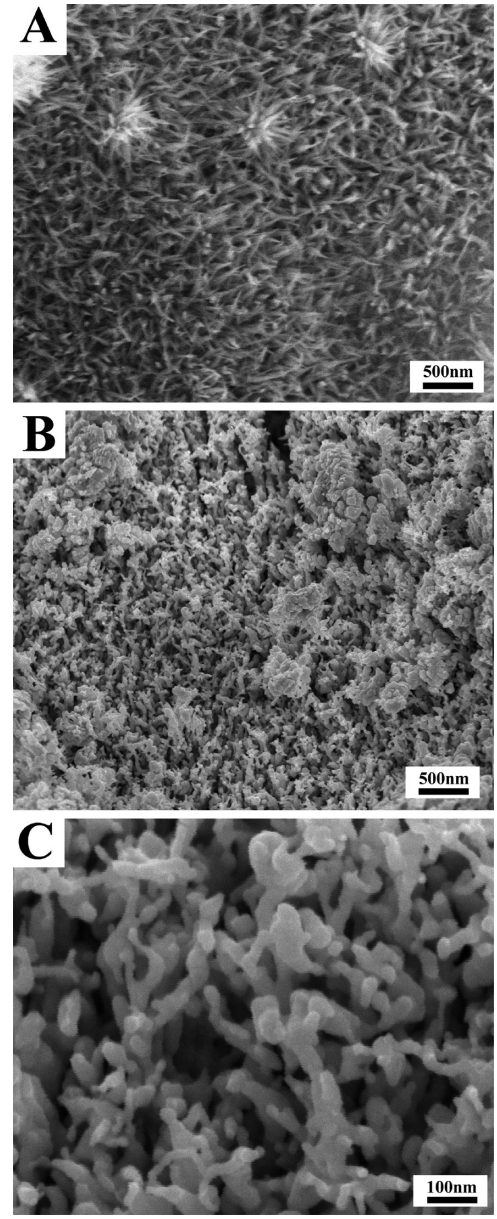

FIGURE 15. SEM images of the $Cu(OH)_2$ NFs before (A) and after (B and C) electrochemical reduction at an Au/$Cu(OH)_2$ NF/Au junction (1 h at −1.65 V).

6. CONCLUSIONS

The electrochemistry of insoluble Ag^I and Cu^{II} fibers has been studied. Because of the significant technological position of AgCN (72), we expect this study to be important in terms of the electrochemical understanding of this material. Some fundamental aspects of the electrochemical reduction of the AgCN−SMA fibers are presented, including their redox

potentials as well as propagation of the metal boundary formed during the electrochemical reduction process. The reduction potential, the nature of the supporting substrate, and the size of the original fibers strongly influence the morphology and size of the Ag^0 nanostructures produced. A range of Ag^0 nanostructures is formed, including nanoprisms, NFs made from the aggregation of large Ag^0 NPs and nanoprisms, and continuous fibers, whose width is tunable between 90 and 500 nm. All of these structures were electrically connected to the substrate, allowing one to make excellent electrical contacts between the two Au electrodes. The thus-produced Ag^0 network could be readily used for the electrical sensing of gases such as ammonia or hydrogen sulfide (3). We expect that the electrochemical synthesis of Ag^0 nanoprisms [via the reduction of solid AgCN fibers and soluble $KAg(CN)_2$ salt] will have a significant impact on the synthesis of Ag^0 nanoprisms via more controllable syntheses. The high tunability offered by electrochemistry to create metallic nanostructures on surfaces provides precise control of the reduction potential. The technique is simple, fast, and applicable to other materials (9−13, 39−42), such as $Cu(OH)_2$ NFs. It allows the formation of electrically connected metallic networks with new interesting geometries that could be used as a form of electrochemical welding. An example was presented with the mechanical and electrical connection of a TEM grid to a Au electrode using AgCN fibers.

This work is also of general interest for the wet-chemical synthesis of metallic nanostructures. Non-zero-valent M^{z+} nanostructures with a well-defined geometry have been used to fabricate metallic nanostructures (9−13). In these cases, depending on the reduction conditions, the geometry of the precursor structure is either preserved or altered. We expect that our study will bring significant knowledge to the understanding of metallic nanostructure syntheses templated with M^{z+} assemblies. Very recent results confirm the versatility of this technique, which can be used to transform semiconducting nanowires into metallic nanostructures and metal/semiconductor heterojunctions.

Acknowledgment. The authors thank the Natural Sciences and Engineering Research Council of Canada and the Center for Self-Assembled Chemical Structures for their financial support.

Supporting Information Available: CV of $KAg(CN)_2$ and $AgCN_{(s)}$, SEM images, size distribution of the AgCN−SMA_{NaCN} NF, and an EDS map of a Au/Ag^0 NF/Au junction. This material is available free of charge via the Internet at http://pubs.acs.org.

REFERENCES AND NOTES

(1) Burda, C.; Chen, X.; Narayanan, R.; El-Sayed, M. A. *Chem. Rev.* **2005**, *105*, 1025–1102.
(2) Kolmakov, A.; Moskovits, M. *Annu. Rev. Mater. Res.* **2004**, *34*, 151–180.
(3) Murray, B. J.; Walter, E. C.; Penner, R. M. *Nano Lett.* **2004**, *4*, 665–670.
(4) Patolsky, F.; Zheng, G.; Lieber, C. M. *Anal. Chem.* **2006**, *78*, 4260–4269.
(5) Yang, F.; Taggart, D. K.; Penner, R. M. *Nano Lett.* **2009**, *9*, 2177–2182.
(6) Lu, W.; Lieber, C. M. *Nat. Mater.* **2007**, *6*, 841–850.
(7) Lin, Y.-F.; Jian, W.-B. *Nano Lett.* **2008**, *8*, 3146–3150.
(8) Al-Mawlawi, D.; Liu, C. Z.; Moskovits, M. *J. Mater. Res.* **1994**, *9*, 1014–1018.
(9) Viau, G.; Piquemal, J.-Y.; Esparrica, M.; Ung, D.; Chakroune, N.; Warmont, F.; Fievet, F. *Chem. Commun.* **2003**, 2216–2217.
(10) Navaladian, S.; Janet, C. M.; Viswanathan, B.; Varadarajan, T. K.; Viswanath, R. P. *J. Phys. Chem. C* **2007**, *111*, 14150–14156.
(11) Lu, X.; Yavuz, M. S.; Tuan, H.-Y.; Korgel, B. A.; Xia, Y. *J. Am. Chem. Soc.* **2008**, *130*, 8900–8901.
(12) Wang, H.; Qi, L. *Adv. Funct. Mater.* **2008**, *18*, 1249–1256.
(13) Lazzara, T. D.; Bourret, G. R.; Lennox, R. B.; van de Ven, T. G. M. *Chem. Mater.* **2009**, *21*, 2020–2026.
(14) Jana, N. R.; Gearheart, L.; Murphy, C. J. *Chem. Commun.* **2001**, 617–618.
(15) Sun, Y.; Xia, Y. *Adv. Mater.* **2002**, *14*, 833–837.
(16) Caswell, K. K.; Bender, C. M.; Murphy, C. J. *Nano Lett.* **2003**, *3*, 667–669.
(17) Halder, A.; Ravishankar, N. *Adv. Mater.* **2007**, *19*, 1854–1858.
(18) Mohanty, P.; Yoon, I.; Kang, T.; Seo, K.; Varadwaj, K. S. K.; Choi, W.; Park, Q.-H.; Ahn, J. P.; Suh, Y. D.; Ihee, H.; Kim, B. *J. Am. Chem. Soc.* **2007**, *129*, 9576–9577.
(19) Reetz, M. T.; Helbig, W. *J. Am. Chem. Soc.* **1994**, *116*, 7401–7402.
(20) Zoval, J. V.; Stiger, R. M.; Biernacki, P. R.; Penner, R. M. *J. Phys. Chem.* **1996**, *100*, 837–844.
(21) Yu, Y.-Y.; Chang, S.-S.; Lee, C.-L.; Wang, C. R. C. *J. Phys. Chem. B* **1997**, *101*, 6661–6664.
(22) Carotenuto, G.; Martorana, B.; Perlo, P.; Nicolais, L. *J. Mater. Chem.* **2003**, *13*, 2927–2930.
(23) Lu, X.; Tuan, H.-Y.; Korgel, B. A.; Xia, Y. *Chem.—Eur. J.* **2008**, *14*, 1584–1591.
(24) Susha, A. S.; Ringler, M.; Ohlinger, A.; Paderi, M.; Li Pira, N.; Carotenuto, G.; Rogach, A. L.; Feldmann, J. *Chem. Mater.* **2008**, *20*, 6169–6175.
(25) Brust, M.; Walker, M.; Bethell, D.; Schiffrin, D. J.; Whyman, R. *Chem. Commun.* **1994**, 801–802.
(26) Goulet, P. J. G.; Lennox, R. B. *J. Am. Chem. Soc.* **2010**, *132*, 9582–9584.
(27) Marin, M. L.; McGilvray, K. L.; Scaiano, J. C. *J. Am. Chem. Soc.* **2008**, *130*, 16572–16584.
(28) Corbierre, M. K.; Beerens, J.; Lennox, R. B. *Chem. Mater.* **2005**, *17*, 5774–5779.
(29) Corbierre, M. K.; Beerens, J.; Beauvais, J.; Lennox, R. B. *Chem. Mater.* **2006**, *18*, 2628–2631.
(30) Zheng, H.; Smith, R. K.; Jun, Y.-W.; Kisielowski, C.; Dahmen, U.; Alivisatos, A. P. *Science* **2009**, *324*, 1309–1312.
(31) Murray, B. J.; Li, Q.; Newberg, J. T.; Menke, E. J.; Hemminger, J. C.; Penner, R. M. *Nano Lett.* **2005**, *5*, 2319–2324.
(32) Liu, R.; Vertegel, A. A.; Bohannan, E. W.; Sorenson, T. A.; Switzer, J. A. *Chem. Mater.* **2001**, *13*, 508–512.
(33) Xu, L.; Guo, Y.; Liao, Q.; Zhang, J.; Xu, D. *J. Phys. Chem. B* **2005**, *109*, 13519–13522.
(34) Xu, L.; Chen, Q.; Xu, D. *J. Phys. Chem. C* **2007**, *111*, 11560–11565.
(35) Nafady, A.; Bond, A. M.; Bilyk, A.; Harris, A. R.; Bhatt, A. I.; O'Mullane, A. P.; De Marco, R. *J. Am. Chem. Soc.* **2007**, *129*, 2369–2382.
(36) Zhao, C.; MacFarlane, D. R.; Bond, A. M. *J. Am. Chem. Soc.* **2009**, *131*, 16195–16205.
(37) Penner, R. M. *J. Phys. Chem. B* **2002**, *106*, 3339–3353.
(38) Xiang, C.; Kung, S.-C.; Taggart, D. K.; Yang, F.; Thompson, M. A.; Guell, A. G.; Yang, Y.; Penner, R. M. *ACS Nano* **2008**, *2*, 1939–1949.
(39) Robinson, R. D.; Sadtler, B.; Demchenko, D. O.; Erdonmez, C. K.; Wang, L.-W.; Alivisatos, A. P. *Science* **2007**, *317*, 355–358.
(40) Wang, D.; Hao, C.; Zheng, W.; Peng, Q.; Wang, T.; Liao, Z.; Yu, D.; Li, Y. *Adv. Mater.* **2008**, *20*, 2628–2632.
(41) Bourret, G. R.; Lennox, R. B. *J. Am. Chem. Soc.* **2010**, *132*, 6657–6659.
(42) Moon, G. D.; Ko, S.; Xia, Y.; Jeong, U. *ACS Nano* **2010**, *4*, 2307–2319.
(43) Bond, A. M.; Scholz, F. *Langmuir* **1991**, *7*, 3197–3204.
(44) Neufeld, A. K.; Madsen, I.; Bond, A. M.; Hogan, C. F. *Chem. Mater.* **2003**, *15*, 3573–3585.
(45) Nafady, A.; O'Mullane, A. P.; Bond, A. M.; Neufeld, A. K. *Chem. Mater.* **2006**, *18*, 4375–4384.

(46) Xiao, W.; Jin, X.; Deng, Y.; Wang, D.; Chen, G. Z. *Chem.—Eur. J.* **2007**, *13*, 604–612.
(47) Hasse, U.; Scholz, F. *Electrochem. Commun.* **2005**, *7*, 173–176.
(48) Scholz, F.; Schröder, U.; Gulaboski, R. *Electrochemistry of Immobilized Particles and Droplets*; Springer: Berlin, 2005.
(49) Bode, D. D.; Andersen, T. N.; Eyring, H. *J. Phys. Chem.* **1967**, *71*, 792–797.
(50) Bozzini, B.; D'Urzo, L.; Mele, C.; Romanello, V. *J. Phys. Chem. C* **2008**, *112*, 6352–6358.
(51) Redmond, P. L.; Hallock, A. J.; Brus, L. E. *Nano Lett.* **2005**, *5*, 131–135.
(52) Malardier-Jugroot, C.; van de Ven, T. G. M.; Whitehead, M. A. *Mol. Simul.* **2005**, *31*, 173–178.
(53) Malardier-Jugroot, C.; van de Ven, T. G. M.; Cosgrove, T.; Richardson, R. M.; Whitehead, M. A. *Langmuir* **2005**, *21*, 10179–10187.
(54) Lide, D. R. *CRC Handbook of Chemistry and Physics*, 90th ed., 2010.
(55) Bowmaker, G. A.; Kennedy, B. J.; Reid, J. C. *Inorg. Chem.* **1998**, *37*, 3968–3974.
(56) The reader might naturally question the safety issues related to the generation of CN^- in neutral aqueous media, which react with H^+ to form toxic HCN gas (HCN $pK_a = 9.21$) as well as the generation of toxic $(CN)_2$ gas. However, $(CN)_2$ has a high solubility in water (>700 $g \cdot L^{-1} \leftrightarrow 13.5\ M \cdot L^{-1}$)[a,b] because of its hydrolysis (see the SI), and HCN is soluble in water.[c] The quantity of HCN and $(CN)_2$ generated in this work is typically 0.25 μmol, corresponding to concentrations of ca. 50 $\mu M \cdot L^{-1}$. Scale-up of this process would require some precautions, and conducting these electrochemical reactions in neutral solutions in a fumehood is strongly advised. (a) Brotherton, T. K.; Lynn, J. W. *Chem. Rev.* **1959**, *59*, 841–883. (b) Yalkowsky, S. H.; He, Y., *Handbook of Aqueous Solubility Data*; CRC Press: Boca Raton, FL, 2003. (c) Corain, B. *Coord. Chem. Rev.* **1982**, *47*, 165–200.
(57) An additional electrochemical process is evident at slightly more anodic potentials. We are unable at the present time to provide an assignment for this peak.
(58) Peterson, M. S. M.; Deutsch, M. *J. Appl. Phys.* **2009**, *106*, 063722.
(59) Jin, R.; Cao, Y.; Mirkin, C. A.; Kelly, K. L.; Schatz, G. C.; Zheng, J. G. *Science* **2001**, *294*, 1901–1903.
(60) Millstone, J. E.; Hurst, S. J.; Metraux, G. S.; Cutler, J. I.; Mirkin, C. A. *Small* **2009**, *5*, 646–664.
(61) Malinsky, M. D.; Kelly, K. L.; Schatz, G. C.; Van Duyne, R. P. *J. Am. Chem. Soc.* **2001**, *123*, 1471–1482.
(62) Haes, A. J.; Zou, S.; Schatz, G. C.; Van Duyne, R. P. *J. Phys. Chem. B* **2004**, *108*, 6961–6968.
(63) Xia, Y.; Xiong, Y.; Lim, B.; Skrabalak, S. E. *Angew. Chem., Int. Ed.* **2009**, *48*, 60–103.
(64) Xue, C.; Mirkin, C. A. *Angew. Chem., Int. Ed.* **2007**, *46*, 2036–2038.
(65) Aherne, D.; Ledwith, D. M.; Gara, M.; Kelly, J. M. *Adv. Funct. Mater.* **2008**, *18*, 2005–2016.
(66) Zei, M. S.; Nakai, Y.; Lehmpfuhl, G.; Kolb, D. M. *J. Electroanal. Chem.* **1983**, *150*, 201–208.
(67) Chen, X. Q.; Saito, T.; Yamada, H.; Matsushige, K. *Appl. Phys. Lett.* **2001**, *78*, 3714–3716.
(68) Jin, S.; Whang, D.; McAlpine, M. C.; Friedman, R. S.; Wu, Y.; Lieber, C. M. *Nano Lett.* **2004**, *4*, 915–919.
(69) Talapin, D. V.; Black, C. T.; Kagan, C. R.; Shevchenko, E. V.; Afzali, A.; Murray, C. B. *J. Phys. Chem. C* **2007**, *111*, 13244–13249.
(70) Wilhelm, S. M.; Tanizawa, Y.; Liu, C.-Y.; Hackerman, N. *Corros. Sci.* **1982**, *22*, 791–805.
(71) Pourbaix, M. *Atlas of Electrochemical Equilibria in Aqueous Solutions*, 2nd English ed.; National Association of Corrosion Engineers: Houston, TX, 1974.
(72) Reyes Cruz, V.; Oropeza, M. T.; Gonzalez, I.; Ponce-De-Leon, C. *J. Appl. Electrochem.* **2002**, *32*, 473–479.

AM100924C